coatings

MDPI

Article

Fabrication and Stability of a Fluorine-Free Superhydrophobic Self-Cleaning Surface on 3003 Aluminum Alloy

Jiahang Zhang [1], Hai Liu [2] and Zhuang Liu [2,*]

[1] School of Pharmacy, Harbin University of Commerce, Harbin 150028, China; zjh199822@sina.com
[2] School of Light Industry, Harbin University of Commerce, Harbin 150028, China; lh3522719129@163.com
* Correspondence: hitprint@163.com

Abstract

To improve the antifouling and self-cleaning performance of 3003 aluminum alloy, a fluorine-free water-repellent surface was fabricated by combining nanosecond laser texturing with subsequent heat treatment. The effects of scanning speed, laser power, pulse frequency, and scanning interval on surface wettability were systematically investigated. Under the optimal conditions of 2700 mm/s, 6 W, 35 kHz, and 20 μm, the surface achieved a maximum static water contact angle of 154.3 ± 0.8°. Surface characterization showed that laser processing generated hierarchical micro-/nano-scale structures, while heat treatment promoted surface chemical evolution associated with enhanced hydrophobicity. The highly water-repellent behavior resulted from the synergistic effect of hierarchical roughness and heat-treatment-induced surface chemical changes. The fabricated surface exhibited effective self-cleaning performance, achieving a SiO_2 removal efficiency of 98.8% under the specified test conditions. In addition, relatively high water repellency was retained after repeated water-impact and tape-peeling tests. These results demonstrate that nanosecond laser texturing combined with heat treatment provides a simple and environmentally friendly strategy for fabricating water-repellent AA3003 surfaces for antifouling and surface-protection applications.

Keywords: AA3003 aluminum alloy; nanosecond laser texturing; fluorine-free surface; superhydrophobicity; self-cleaning; wettability retention

1. Introduction

Aluminum and its alloys are widely used in aerospace, transportation, architectural decoration, electronic devices, heat exchangers, and marine engineering because of their low density, high specific strength, favorable processability, and corrosion resistance. Among them, 3003 aluminum alloy is a typical Al–Mn alloy with good formability, weldability, and corrosion resistance, and is extensively used in heat exchangers, storage tanks, packaging materials, and lightweight structural components. During service, however, aluminum surfaces are frequently exposed to moisture, dust, and airborne contaminants. The accumulation of water and contaminants not only reduces surface cleanliness but may also accelerate localized degradation under humid or corrosive environments. Therefore, the fabrication of water-repellent and self-cleaning surfaces on 3003 aluminum alloy is of considerable practical interest [1–3].

Superhydrophobic surfaces are generally characterized by a static water contact angle (WCA) greater than 150°. Inspired by natural surfaces such as lotus leaves and water strider legs, artificial superhydrophobic surfaces have attracted extensive attention because of their

Check for updates

Academic Editor: Anita Ioana Visan

Received: 6 June 2026
Revised: 12 July 2026
Accepted: 17 July 2026
Published: 17 August 2026

Copyright: © 2026 by the authors. Licensee MDPI, Basel, Switzerland. This article is an open access article distributed under the terms and conditions of the Creative Commons Attribution (CC BY) license.

potential applications in self-cleaning, antifouling, anti-adhesion, drag reduction, and surface protection [4–7]. The water-repellent behavior of these surfaces typically originates from the combined effects of hierarchical micro-/nano-scale structures and low-surface-energy surface chemistry. For metallic materials, suitable surface roughness alone is often insufficient because freshly formed oxide and hydroxylated surfaces usually possess relatively high surface energy. Consequently, both surface morphology and surface chemistry play important roles in determining wettability [8–10].

Various methods have been developed to fabricate superhydrophobic metallic surfaces, including chemical etching, electrochemical deposition, anodization, sol–gel processing, spraying, and laser texturing [11–16]. Among these approaches, laser processing has attracted considerable interest because of its non-contact nature, high precision, mask-free fabrication capability, and excellent process controllability. In particular, nanosecond laser processing offers relatively high efficiency and low cost, making it suitable for large-area surface texturing [17–19].

During nanosecond laser irradiation, rapid energy deposition induces ablation, melting, vaporization, particle redeposition, and surface oxidation, generating micro-/nano-scale structures that provide the roughness required for water repellency. However, freshly laser-textured aluminum surfaces are usually hydrophilic because laser processing exposes high-energy oxide surfaces and generates polar oxygen-containing species. Therefore, post-treatment methods such as ambient aging or heat treatment are commonly employed to promote the transition from hydrophilicity to hydrophobicity [20–23].

The functions of laser texturing and heat treatment are complementary. Laser processing primarily constructs hierarchical rough structures, whereas subsequent heat treatment promotes changes in surface chemistry and reduces the apparent surface free energy. Previous studies have suggested that moderate heating can accelerate the adsorption or rearrangement of airborne carbon-containing species on textured surfaces, thereby facilitating the development of hydrophobicity [24–27]. As a result, the combination of laser-induced roughness and heat-treatment-associated surface chemical evolution provides an effective fluorine-free route for preparing superhydrophobic metallic surfaces.

Although laser-induced superhydrophobicity has been widely studied on aluminum alloys and other metallic substrates, comparatively limited attention has been paid to fluorine-free superhydrophobic modification of 3003 aluminum alloy. Furthermore, the effects of key nanosecond laser parameters, including scanning speed, laser power, pulse frequency, and scanning interval, on surface morphology and wettability have not been systematically clarified for this alloy. Since these parameters collectively influence energy input, thermal accumulation, ablation behavior, and texture continuity, identifying suitable processing conditions is essential for achieving highly water-repellent surfaces.

In this study, a fluorine-free strategy combining nanosecond laser texturing and subsequent heat treatment was employed to fabricate superhydrophobic surfaces on 3003 aluminum alloy. The effects of scanning speed, laser power, pulse frequency, and scanning interval on wettability and surface morphology were systematically investigated. Surface roughness, morphology, elemental composition, and functional-group evolution were characterized to elucidate the respective roles of laser-generated hierarchical structures and heat-treatment-associated surface chemical changes. In addition, the self-cleaning performance and wettability retention under water impact, tape peeling, and ambient storage were evaluated.

2. Materials and Methods

2.1. Materials and Sample Pretreatment

Commercial 3003 aluminum alloy sheets were used as substrates in this study. The samples were cut into rectangular specimens with dimensions of 10 mm × 10 mm × 0.5 mm. Before laser processing, the samples were ultrasonically cleaned sequentially in absolute ethanol and deionized water for 10 min each (40 kHz, 240 W) to remove surface contaminants and residual particles. Subsequently, the samples were dried at 60 °C for 20 min before laser texturing.

2.2. Biomimetic Inspiration from Chelidonium Majus Leaf Surface

The hierarchical surface morphology of Chelidonium majus leaves was selected as the biomimetic prototype for designing water-repellent structures, as illustrated in Figure 1. Natural leaf surfaces typically contain irregular papillary, rod-like, and needle-like microstructures, which increase surface roughness and facilitate air trapping beneath water droplets.

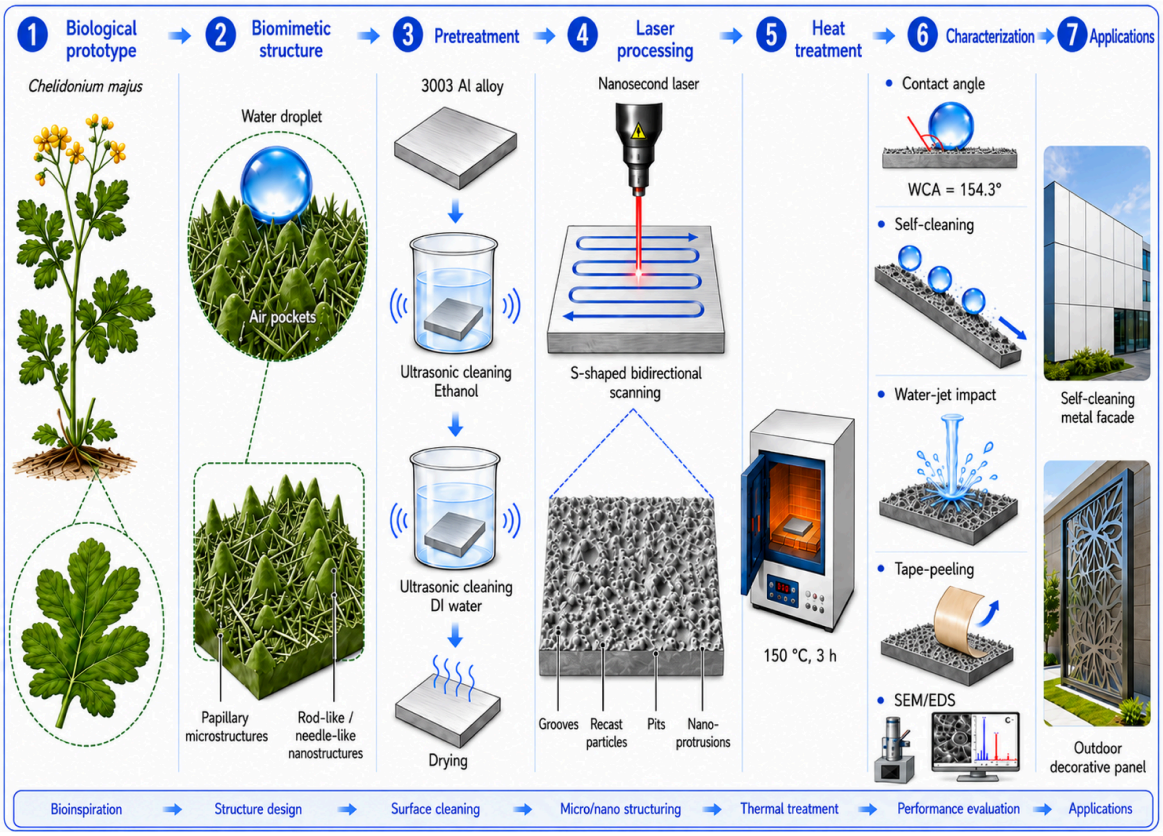


Figure 1. Schematic illustration of the fabrication process of a Chelidonium majus-inspired superhydrophobic surface on 3003 aluminum alloy, including bioinspiration, surface pretreatment, nanosecond laser texturing, heat treatment, and performance characterization.

Inspired by this hierarchical architecture, nanosecond laser texturing was employed to construct multiscale rough structures on 3003 aluminum alloy. Although a regular S-shaped scanning strategy was adopted during laser processing, the final surface morphology was generated through complex laser–material interactions, including ablation, localized melting, melt redistribution, rapid solidification, particle ejection, and oxidation. These processes resulted in the formation of irregular grooves, pits, resolidified particles, and nanoscale protrusions, providing the structural foundation for water repellency.

2.3. Nanosecond Laser Processing and Heat Treatment

Laser surface modification was performed using a nanosecond fiber laser system with a wavelength of 1064 nm and a pulse duration of 10 ns. The laser beam was delivered through a galvanometric scanning system, and the approximate laser spot radius was 50 μm. An S-shaped bidirectional scanning strategy was adopted to ensure uniform coverage of the selected processing region.

Single-factor experiments were designed to investigate the effects of four key laser parameters, including scanning speed, laser power, pulse frequency, and scanning interval, on surface wettability. The initial processing parameters were set as follows: scanning speed of 1000 mm/s, laser power of 12 W, pulse frequency of 30 kHz, and scanning interval of 30 μm. During each experiment, only one parameter was varied while the remaining parameters were maintained constant.

The scanning interval was defined as the center-to-center distance between two adjacent laser scanning tracks. After laser processing, the samples were ultrasonically cleaned in deionized water for 10 min to remove loosely attached debris generated during ablation.

2.4. Heat Treatment

To promote the hydrophobic transition of the laser-textured surfaces, post-processing heat treatment was performed in an electric thermostatic drying oven. The laser-treated samples were heated at 150 °C for 3 h and subsequently cooled naturally to room temperature.

The combined laser-texturing and heat-treatment process was used to simultaneously regulate surface morphology and surface chemical characteristics. Laser irradiation mainly generated hierarchical rough structures, while heat treatment promoted surface chemical evolution associated with wettability transition.

2.5. Surface Morphology, Roughness, and Chemical Characterization

The surface morphology of the laser-treated samples was initially examined using an optical microscope (HG1501T, maximum magnification: 200×) to evaluate the uniformity of laser-induced textures.

Selected samples with improved wettability were further characterized by scanning electron microscopy (SEM) and energy-dispersive spectroscopy (EDS). SEM observations were conducted at an accelerating voltage of 15 kV with magnifications of 5.00 k×, 10.00 k×, and 30.0 k×. EDS analysis was performed to compare the elemental compositions of laser-textured surfaces before and after heat treatment.

Three-dimensional surface profiles and roughness parameters were measured to quantitatively evaluate the surface topographical changes induced by laser processing and heat treatment. The arithmetic mean height (Sa), root–mean–square height (Sq), and maximum height (Sz) were used to characterize surface roughness.

Fourier-transform infrared spectroscopy (FTIR) was employed to analyze the evolution of surface functional groups after laser processing, ambient aging, and heat treatment. The spectra were collected in the range of 4000–1000 cm^{-1} to investigate the changes associated with oxygen-containing and carbon-containing surface species.

2.6. Wettability Measurement

Static water contact angle (WCA) measurements were performed using a contact angle goniometer (JCJ-360A). Deionized water droplets with a volume of 10 μL were used for all measurements.

For each sample, WCAs were measured at three randomly selected positions, and the results are presented as the mean ± standard deviation. A static WCA greater than 150° was considered as the criterion for superhydrophobicity in this study.

2.7. Powder-Based Self-Cleaning Test

The self-cleaning performance was evaluated using SiO_2 powder as a model contaminant. Before testing, SiO_2 powder with an average particle size of approximately 1 μm was dried to minimize the influence of adsorbed moisture and particle agglomeration.

The powder was uniformly distributed on both untreated and laser-textured/heat-treated AA3003 surfaces. The samples were placed at an inclination angle of approximately 10°. Deionized water droplets were subsequently applied using a 20 μL microsyringe.

Each droplet had a volume of approximately 10–15 μL and was gradually applied to the contaminated region. The sequential removal behavior was recorded during the cleaning process. The residual SiO_2-covered area after cleaning was quantified using ImageJ version 1.54d software, and the removal efficiency was calculated according to:

$$\eta = \left(1 - \frac{A_r}{A_0}\right) \times 100\%$$

where A_0 represents the initial contaminated area and A_r represents the residual contaminated area after cleaning.

2.8. Repeated Water-Impact Test

The wettability retention under repeated water impact was evaluated by a gravity-driven water-impact experiment. Approximately 400 mL of deionized water was released vertically from a height of 30 ± 2 cm above the sample surface during each impact cycle.

After predetermined numbers of impact cycles, the static WCA was measured to evaluate the variation in surface wettability. Three independent measurements were conducted for each condition, and the results are expressed as the mean ± standard deviation.

The theoretical impact velocity before contacting the surface was estimated using:

$$v = \sqrt{2gh}$$

where v is the theoretical impact velocity, g is gravitational acceleration, and h is the release height.

2.9. Tape-Peeling Test

Mechanical stability was evaluated using a repeated tape-peeling test. Adhesive tape with a width of 1.5 cm was attached to the laser-textured and heat-treated AA3003 surface.

A glass plate (10 cm × 10 cm) loaded with approximately 2 L of water was placed on the tape for 2 min to provide uniform contact pressure between the adhesive layer and the surface. The tape was subsequently removed at an approximately constant peeling rate.

After predetermined peeling cycles, static WCAs were measured at three different positions. The mean value and standard deviation were calculated to evaluate the retention of water repellency after mechanical disturbance.

3. Results and Discussion

3.1. Effect of Scanning Speed on Surface Wettability

The effect of scanning speed on the wettability of laser-textured 3003 aluminum alloy surfaces was investigated at a fixed laser power of 12 W, pulse frequency of 30 kHz, and scanning interval of 30 μm. After laser texturing, all samples were heat-treated at 150 °C for 3 h. Because the as-laser-textured surfaces were superhydrophilic, the following discussion focuses on the heat-treated samples. The WCA values are expressed as the mean ± standard deviation of three independent measurements.

As shown in Figure 2a, the WCA initially increased and subsequently decreased with increasing scanning speed. When the scanning speed increased from 500 to 3000 mm/s, the WCA increased from 144.5 ± 1.2° to 149.4 ± 0.6°. A further increase in scanning speed resulted in a marked decrease in WCA. At 4500 and 5000 mm/s, the WCA values decreased to 141.5 ± 1.2° and 140.7 ± 4.9°, respectively. The comparatively large standard deviation at 5000 mm/s also suggests that excessively high scanning speeds produced less spatially uniform wetting behavior.

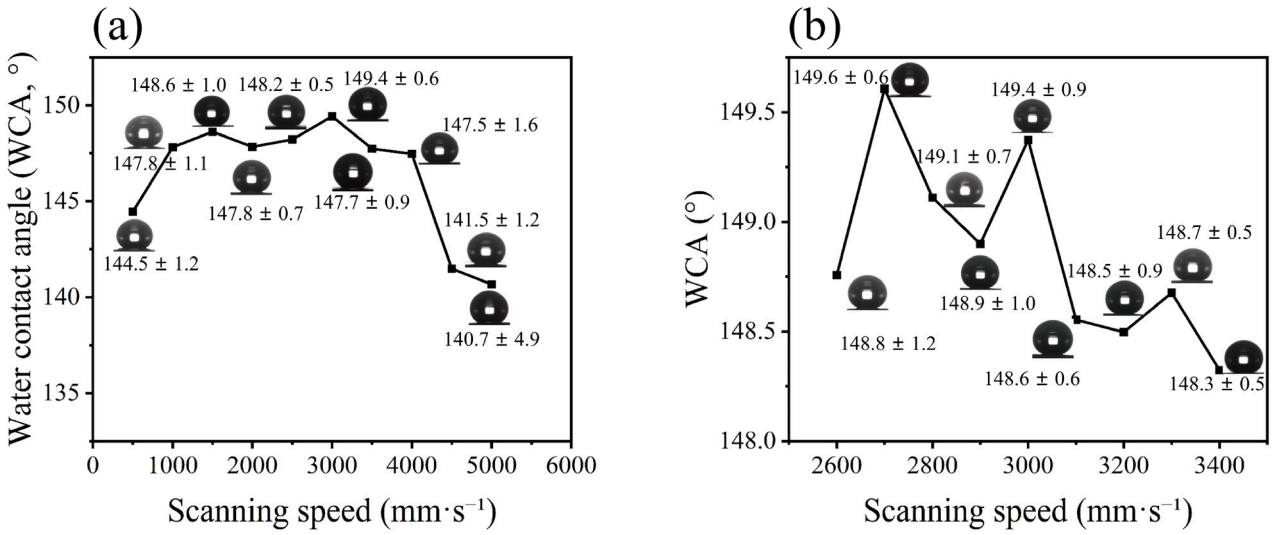


Figure 2. Effect of scanning speed on the water contact angle of 3003 aluminum alloy surfaces: (**a**) 500–5000 mm/s; (**b**) 2600–3400 mm/s.

The corresponding surface morphologies are shown in Figure 3. At a low scanning speed of 500 mm/s, the prolonged laser–material interaction resulted in excessive energy input per unit area, leading to severe ablation, melting, and resolidification. The resulting surface texture was irregular and non-uniform, which was not favorable for supporting water droplets. When the scanning speed increased to 3000 mm/s, the laser energy input became more appropriate, and relatively continuous rough textures with pits and protrusions were formed. This morphology was more favorable for reducing the actual solid–liquid contact fraction, thereby increasing the apparent WCA. In contrast, at 5000 mm/s, the laser–material interaction time was too short, resulting in insufficient ablation and discontinuous surface structures. The reduced texture coverage weakened the droplet-supporting capability, leading to lower hydrophobicity.

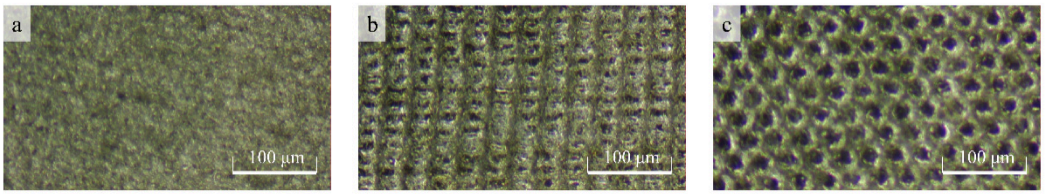


Figure 3. Surface morphologies of 3003 aluminum alloy at different scanning speeds (200×): (**a**) 500 mm/s; (**b**) 3000 mm/s; (**c**) 5000 mm/s.

To further identify the suitable scanning speed, refined experiments were carried out in the range of 2600–3400 mm/s, as shown in Figure 2b. The WCA values remained within 148.3–149.6°, indicating relatively stable hydrophobicity in this range. The maximum WCA of 149.6 ± 0.6° was obtained at 2700 mm/s. Therefore, 2700 mm/s was selected as the preferred scanning speed for subsequent experiments.

3.2. Effect of Laser Power on Surface Wettability

Based on the selected scanning speed of 2700 mm/s, the effect of laser power on surface wettability was investigated at a fixed pulse frequency of 30 kHz and scanning interval of 30 μm. Laser power regulates the energy delivered to the substrate and therefore affects the extent of ablation, melting–resolidification, material redeposition, oxidation, and surface-feature evolution.

As shown in Figure 4a, the WCA remained relatively high when the laser power was between 3 and 12 W. Specifically, the WCA increased slightly from 150.0 ± 0.8° at 3 W to 150.5 ± 1.0° at 6 W and then remained close to 150° at 9 and 12 W. When the laser power exceeded 15 W, the WCA progressively decreased. At 24 W, the WCA decreased to 142.4 ± 1.7°, indicating that excessive laser energy input was unfavorable for maintaining high apparent hydrophobicity.

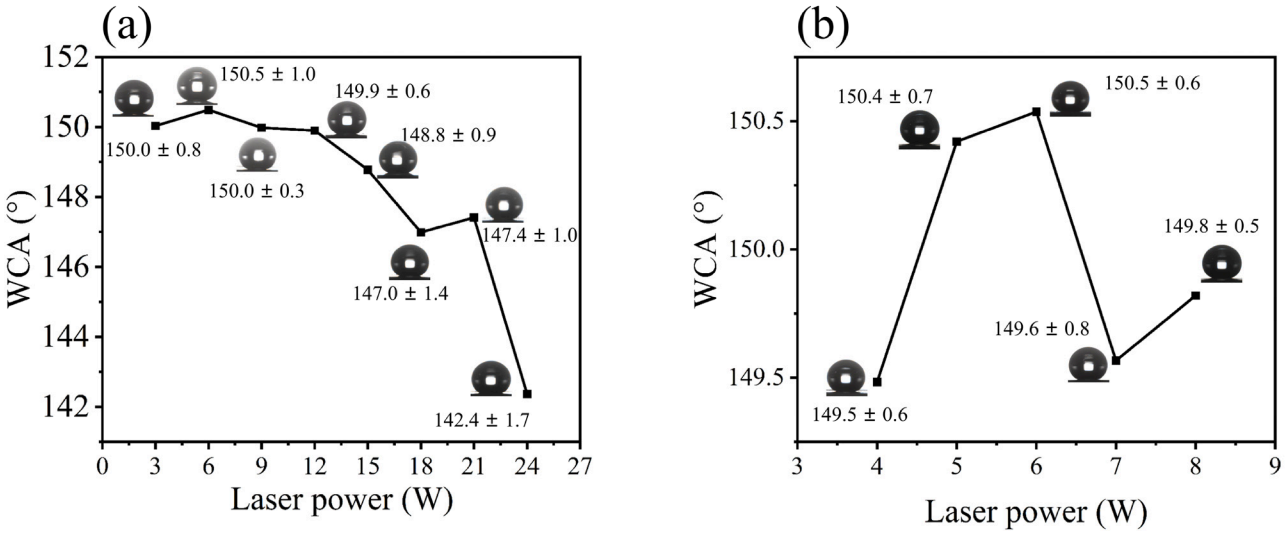


Figure 4. Effect of laser power on the water contact angle of 3003 aluminum alloy surfaces: (**a**) 3–24 W; (**b**) 4–8 W.

Refined experiments were subsequently conducted between 4 and 8 W, as shown in Figure 4b. The WCA increased from 149.5 ± 0.6° at 4 W to 150.5 ± 0.6° at 6 W. Further increasing the laser power to 7 and 8 W resulted in WCA values of 149.6 ± 0.8° and 149.8 ± 0.5°, respectively. Therefore, 6 W was selected because it produced the highest mean WCA within the refined range while maintaining a relatively small standard deviation.

Representative optical morphologies are shown in Figure 5. At 6 W, the laser energy was sufficient to induce effective ablation and material redistribution, resulting in comparatively uniform surface features. The resulting pits, protrusions, and resolidified regions increased the topographical complexity of the surface and may have promoted the retention of air beneath the water droplet.

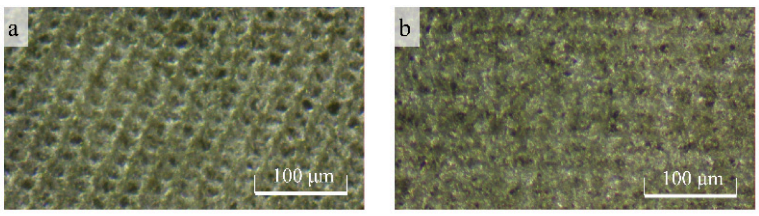


Figure 5. Surface morphologies of 3003 aluminum alloy at different laser powers (200×): (**a**) 6 W; (**b**) 24 W.

At 24 W, the substantially higher energy input intensified ablation and melting–resolidification. The optical morphology indicates increased structural coalescence and reduced uniformity, consistent with extensive melt redistribution and repeated thermal modification. Under such conditions, previously formed features may be partially merged, flattened, or obscured by resolidified material. These changes can reduce the effective air-retaining volume of the texture and increase the effective solid–liquid contact fraction, thereby decreasing the apparent WCA.

This non-monotonic response is consistent with previous studies showing that an appropriate laser-energy range is required to generate effective water-repellent topographies. Excessive incident energy may promote over-ablation, pronounced melt redistribution, and coalescence of surface features, whereas insufficient energy may fail to generate adequate texture coverage [20,28]. The present results therefore suggest that laser power regulates wettability through a balance between effective surface-feature formation and excessive thermal modification.

Overall, laser power influenced surface wettability by balancing effective texture formation and excessive thermal damage. Under the present experimental conditions, 6 W provided suitable energy input and was used in the following experiments.

3.3. Effect of Pulse Frequency on Surface Wettability

The effect of pulse frequency on surface wettability was investigated using a scanning speed of 2700 mm/s, a laser power of 6 W, and a scanning interval of 30 μm. At a constant nominal average laser power, the single-pulse energy is inversely proportional to pulse frequency (Ep = P/f), whereas the center-to-center pulse spacing along the scanning direction is given by s = v/f. Pulse frequency therefore simultaneously affects single-pulse energy, longitudinal pulse overlap, and the temporal interval between successive laser pulses.

Under the present conditions, increasing the pulse frequency from 20 to 80 kHz reduced the nominal single-pulse energy from approximately 0.30 to 0.075 mJ and decreased the pulse spacing from approximately 135 to 33.8 μm. At 35 kHz, the nominal single-pulse energy and pulse spacing were approximately 0.171 mJ and 77.1 μm, respectively. These changes provide a physical basis for the observed frequency-dependent surface morphology and wettability.

As shown in Figure 6a, the WCA initially increased slightly and then decreased sharply as the pulse frequency increased from 20 to 80 kHz. At 20–40 kHz, the WCA remained above 150°, and the highest value in the preliminary experiment was obtained at 40 kHz, reaching 151.7 ± 0.9°. When the pulse frequency increased to 50 kHz, the WCA decreased to 146.1 ± 1.6°. Further increases to 60, 70, and 80 kHz resulted in WCA values of 142.5 ± 0.5°, 136.7 ± 1.8°, and 90.8 ± 1.2°, respectively. These results demonstrate that excessively high pulse frequencies were unfavorable for maintaining the highly water-repellent state.

Refined experiments were conducted between 31 and 39 kHz, as shown in Figure 6b. The WCA remained above 150° throughout this range. The highest mean WCA, 152.3 ± 0.9°, was obtained at 35 kHz, whereas the WCA values at 37 and 39 kHz were 151.4 ± 0.7° and 151.8 ± 0.6°, respectively. Accordingly, 35 kHz was selected as the preferred pulse frequency for the subsequent experiments.

The corresponding optical morphologies are shown in Figure 7. At 20 kHz, the relatively high single-pulse energy and large pulse spacing promoted pronounced but comparatively discrete material removal and redistribution. This combination may produce local heterogeneity because neighboring irradiated regions do not overlap sufficiently to form a uniformly modified surface.

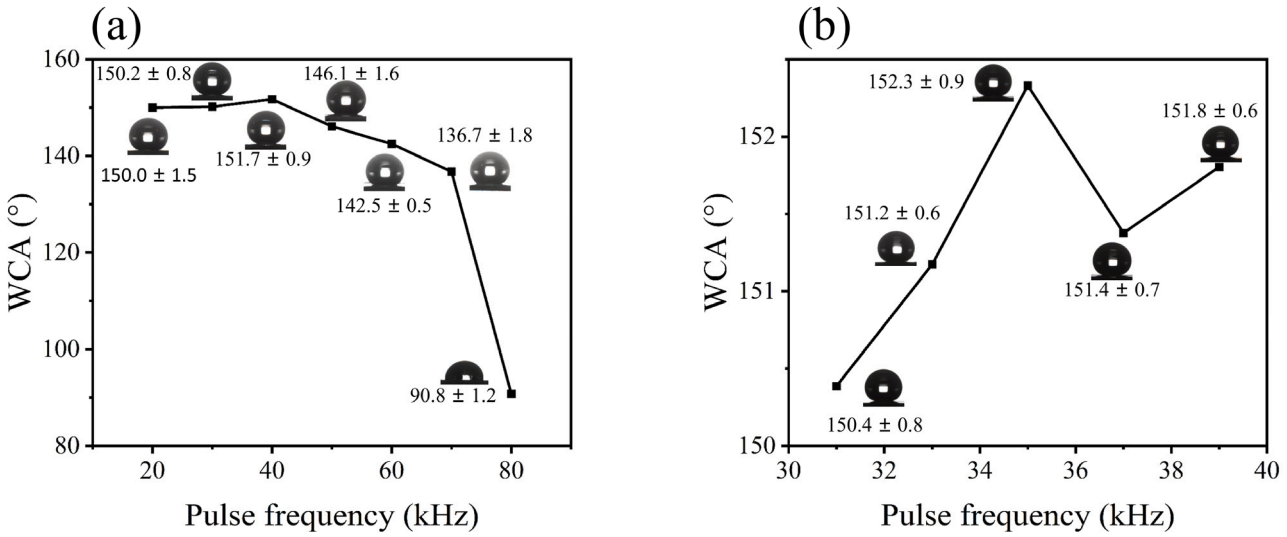


Figure 6. Effect of laser pulse frequency on the water contact angle of 3003 aluminum alloy surfaces: (**a**) 20–80 kHz; (**b**) 31–39 kHz.

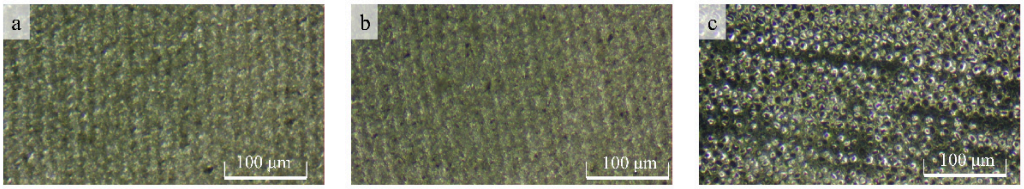


Figure 7. Surface morphologies of 3003 aluminum alloy at different pulse frequencies (200×): (**a**) 20 kHz; (**b**) 40 kHz; (**c**) 80 kHz.

The morphology obtained at 40 kHz is representative of the favorable intermediate-frequency range. In this range, the combination of moderate single-pulse energy and increased pulse density produced more continuous and uniformly distributed surface features. Such a morphology is expected to provide more consistent texture coverage and a lower effective solid–liquid contact fraction.

At 80 kHz, the lower single-pulse energy was accompanied by a much smaller pulse spacing and a shorter temporal interval between successive pulses. Although the total nominal energy delivered per unit scanning length remained governed by the average power and scanning speed, the altered spatial and temporal distribution of the pulses may have promoted repeated reheating, local remelting, and smoothing of previously generated features. At the same time, the reduced single-pulse energy may have limited the extent of effective material removal. The combined effect produced a surface morphology that was less favorable for air retention and corresponded to the substantially lower WCA.

A recent response-surface study on laser-textured 6061 aluminum alloy also identified repetition frequency as an important processing variable and selected an intermediate frequency of 40 kHz as part of its preferred parameter combination [29]. More recent work on coating-free laser-textured aluminum surfaces has further emphasized the coupled effects of laser fluence, pulse overlap, and scanning parameters on the wetting state [30]. Although direct numerical comparison is inappropriate because of differences in laser pulse duration, alloy composition, and texture geometry, these studies support the present interpretation that an intermediate frequency provides a more favorable balance between single-pulse energy and pulse overlap.

Therefore, pulse frequency affected surface wettability by changing both the energy of individual pulses and their spatial–temporal overlap. Under the present experimental

conditions, 35 kHz was selected as the preferred frequency for the subsequent scanning-interval experiments.

3.4. Effect of Scanning Interval on Surface Wettability

The effect of scanning interval on surface wettability was investigated at a scanning speed of 2700 mm/s, laser power of 6 W, and pulse frequency of 35 kHz. The scanning interval, also referred to as hatch spacing, determines the transverse overlap between adjacent laser tracks and therefore affects the processed-area fraction, texture continuity, repeated irradiation, and spatial uniformity of the resulting surface.

As shown in Figure 8a, the WCA initially increased and subsequently decreased as the scanning interval increased from 1 to 50 μm. At the smallest interval of 1 μm, the WCA was 147.8 ± 0.4°. Increasing the interval to 10 and 20 μm increased the WCA to 151.4 ± 1.0° and 153.7 ± 1.2°, respectively. Further increases to 30, 40, and 50 μm reduced the WCA to 151.3 ± 0.9°, 148.7 ± 0.6°, and 147.1 ± 0.2°, respectively. These results indicate that neither extremely dense nor excessively sparse laser tracks were favorable for maximizing the apparent WCA.

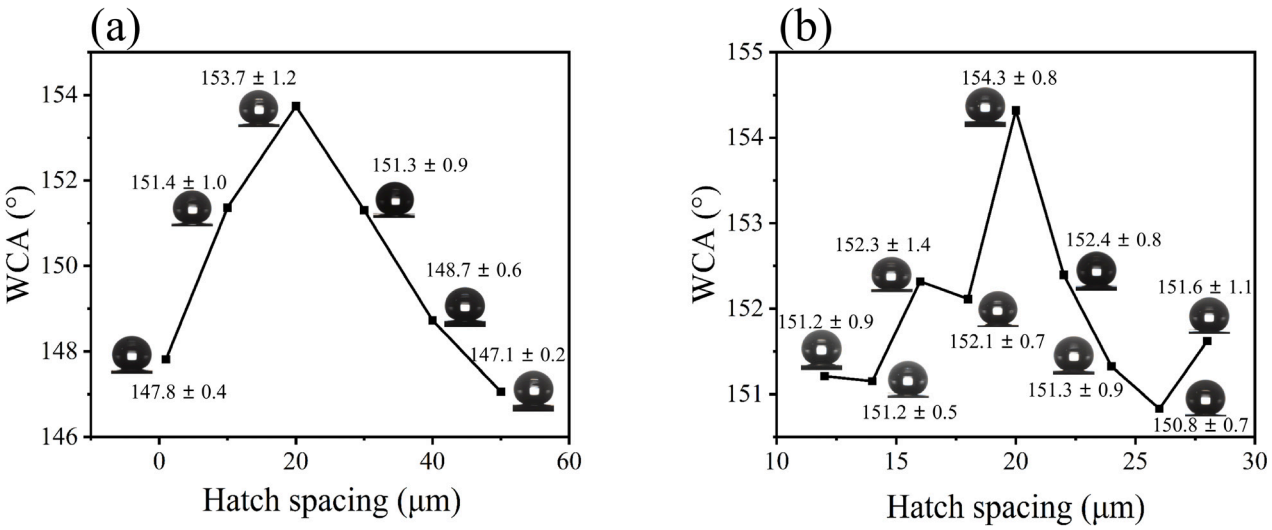


Figure 8. Effect of scanning interval on the water contact angle of 3003 aluminum alloy surfaces: (**a**) 1–50 μm; (**b**) 10–30 μm.

Refined experiments were subsequently conducted between 12 and 28 μm, as shown in Figure 8b. The WCA increased from 151.2 ± 0.9° at 12 μm to a maximum of 154.3 ± 0.8° at 20 μm. When the scanning interval was further increased to 22, 24, 26, and 28 μm, the WCA values decreased to 152.4 ± 0.8°, 151.3 ± 0.9°, 150.8 ± 0.7°, and 151.6 ± 1.1°, respectively. Therefore, 20 μm was selected as the preferred scanning interval.

The corresponding optical morphologies are shown in Figure 9. At a scanning interval of 1 μm, the extremely high overlap between adjacent tracks caused repeated irradiation of the same surface regions. This condition promoted extensive material accumulation, feature coalescence, and local non-uniformity. Although the surface was densely modified, excessive repeated irradiation may have reduced the effectiveness of the resulting texture for retaining air beneath the water droplet.

At 20 μm, adjacent tracks maintained sufficient overlap to produce comparatively continuous and uniformly distributed pits and protrusions while avoiding excessive repeated irradiation. This combination provided broad texture coverage together with distinct surface features and corresponded to the highest WCA. The morphology therefore suggests a favorable balance between texture continuity, effective solid fraction, and air-retaining capacity.

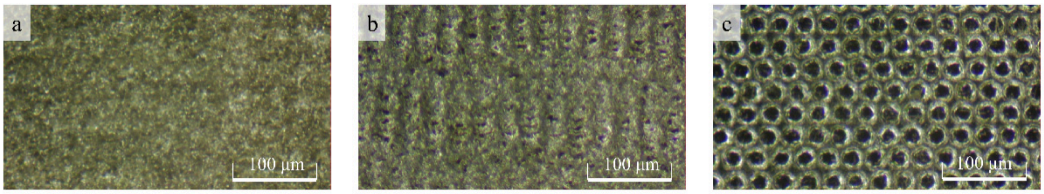


Figure 9. Surface morphologies of 3003 aluminum alloy at different scanning intervals (200×): (**a**) 1 μm; (**b**) 20 μm; (**c**) 50 μm.

At 50 μm, the separation between adjacent tracks was comparatively large relative to the effectively modified track width. The resulting texture became sparser and less continuous, increasing the likelihood that the droplet contacted incompletely processed or relatively flat regions. Consequently, the effective solid–liquid contact fraction increased and the apparent WCA decreased.

Previous research has similarly demonstrated that groove or hatch spacing strongly affects the wetting behavior of laser-textured aluminum surfaces. Volpe et al. reported that, at relatively small groove spacing, the fraction of textured surface and the volume of air retained within the texture became important determinants of the apparent wetting state [21]. Farhan et al. also showed that line spacing affected both the wettability and the number of water droplets required for self-cleaning on laser-textured 6061 aluminum alloy [29]. These observations are consistent with the present result that an intermediate scanning interval provides a more favorable balance between continuous texture coverage and excessive track overlap.

3.5. Summary of Parameter Selection

Based on the above single-factor experiments, the preferred laser-processing parameters for fabricating hydrophobic 3003 aluminum alloy surfaces were determined as follows: scanning speed of 2700 mm/s, laser power of 6 W, pulse frequency of 35 kHz, and scanning interval of 20 μm. Among these parameters, scanning speed mainly affected the laser–material interaction time and energy input per unit area; laser power controlled the overall ablation intensity; pulse frequency regulated single-pulse energy, pulse overlap, and heat accumulation; and scanning interval determined the overlap and coverage of adjacent laser tracks.

Under the selected parameter combination, the heat-treated 3003 aluminum alloy surface exhibited a maximum WCA of 154.3 ± 0.8°, indicating that a superhydrophobic surface could be obtained through appropriate control of laser-processing parameters and subsequent heat treatment. The preferred laser-processing parameters and their corresponding maximum WCA values are summarized in Table 1.

Table 1. Summary of the preferred laser-processing parameters and corresponding WCA values.

Parameter	Investigated Range	Refined Range	Preferred Value	Maximum WCA/°
Scanning speed	500–5000 mm/s	2600–3400 mm/s	2700 mm/s	149.6 ± 0.6
Laser power	3–24 W	4–8 W	6 W	150.5 ± 0.6
Pulse frequency	20–80 kHz	31–39 kHz	35 kHz	152.3 ± 0.9
Scanning interval	1–50 μm	12–28 μm	20 μm	154.3 ± 0.8

3.6. Surface Morphology and Roughness Analysis

The surface morphology and roughness of 3003 aluminum alloy were examined under the selected processing conditions: a scanning speed of 2700 mm/s, laser power of 6 W, pulse frequency of 35 kHz, and scanning interval of 20 μm. After heat treatment at 150 °C

for 3 h, the laser-textured surface exhibited a water contact angle of 154.3 ± 0.8°, confirming the formation of a superhydrophobic surface.

Figure 10(a1,a2) presents the SEM images of the laser-textured surface. At low magnification, the surface is covered by continuous but irregular rough structures composed of strip-like features, pits, and protrusions. These structures result from laser-induced ablation, localized melting, material ejection, and rapid resolidification. The enlarged image in Figure 10(a2) further shows that the protrusions are decorated with finer secondary features, producing a multiscale surface morphology. This rough architecture increases surface heterogeneity and provides favorable geometrical conditions for air retention beneath water droplets, thereby reducing the effective solid–liquid contact area. Similar effects of laser-induced multiscale structures on the wettability of aluminum alloy surfaces have been reported previously [31].

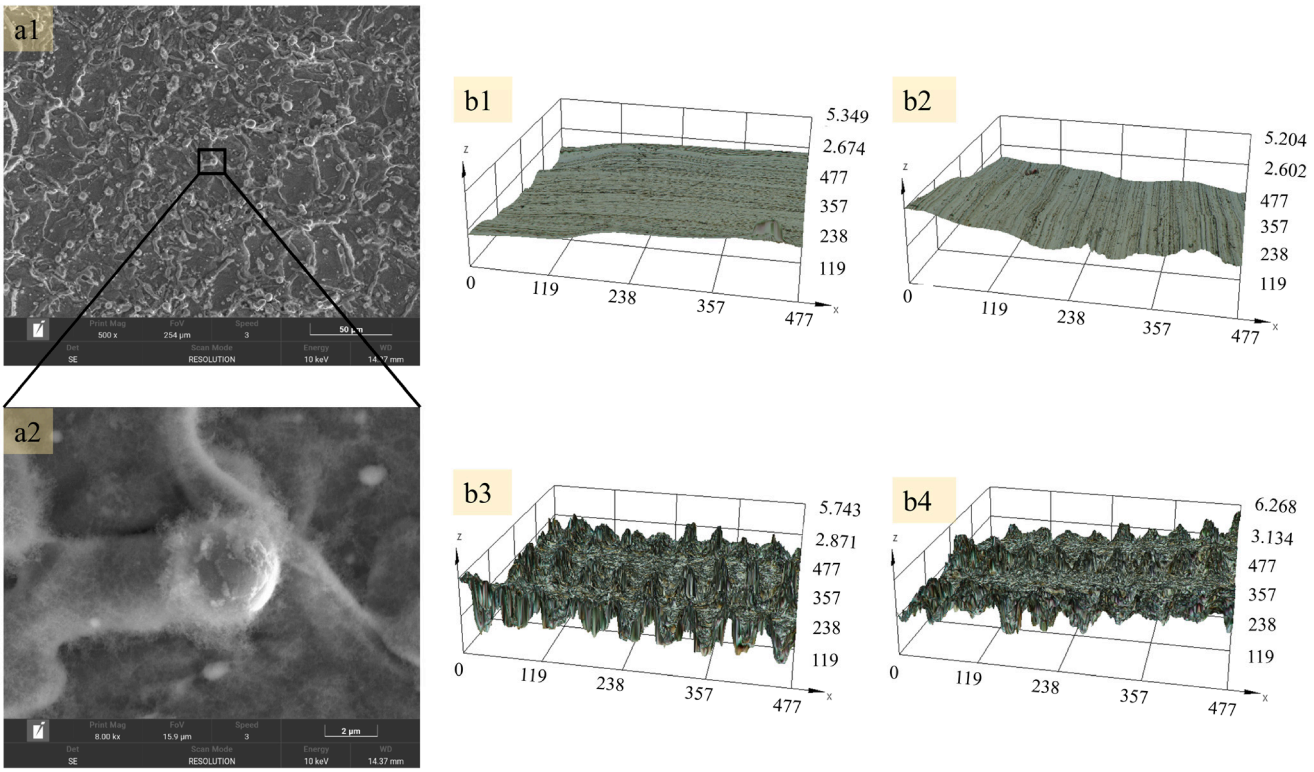


Figure 10. SEM images and three-dimensional surface profiles of 3003 aluminum alloy surfaces: (**a1**) low-magnification SEM image of the laser-textured surface; (**a2**) enlarged SEM image of the selected region in (**a1**); (**b1**) untreated sample; (**b2**) heat-treated sample; (**b3**) laser-treated sample; and (**b4**) laser- and heat-treated sample.

To further quantify the surface morphology, three-dimensional surface profiles were obtained for different samples, as shown in Figure 10(b1–b4). The untreated aluminum alloy surface exhibits a relatively flat morphology with only slight surface undulations. After heat treatment alone, the surface profile remains similar to that of the untreated sample, indicating that heat treatment does not obviously change the original surface topography. In contrast, the laser-treated surface shows a much rougher three-dimensional morphology with pronounced peak–valley structures. The strong surface fluctuation observed in Figure 10(b3) is consistent with the irregular ablation morphology observed in the SEM images. After heat treatment, the laser-textured surface still maintains obvious rough features, as shown in Figure 10(b4), suggesting that the laser-induced rough structure is largely preserved during the heat treatment process.

The roughness parameters further confirm this tendency. The untreated aluminum alloy surface shows relatively low roughness, with Sa, Sq, and Sz values of 0.31 ± 0.05 μm, 0.39 ± 0.05 μm, and 2.59 ± 0.77 μm, respectively. After heat treatment alone, these values change slightly to 0.27 ± 0.03 μm, 0.35 ± 0.02 μm, and 2.56 ± 0.51 μm, respectively, confirming that heat treatment itself has limited influence on the surface roughness of the original aluminum alloy. In contrast, laser processing significantly increases the surface roughness. The Sa and Sq values increase to 0.42 ± 0.02 μm and 0.59 ± 0.003 μm, respectively, while the Sz value increases to 5.49 ± 0.82 μm. The increased Sz value indicates the formation of more pronounced peak–valley structures after laser ablation.

After heat treatment of the laser-textured surface, the Sa, Sq, and Sz values are 0.36 ± 0.04 μm, 0.51 ± 0.06 μm, and 4.70 ± 0.41 μm, respectively. Although these values are slightly lower than those of the laser-treated surface before heat treatment, they are still clearly higher than those of the untreated and heat-treated samples. This result indicates that the rough hierarchical morphology is mainly generated by laser processing and remains largely retained after heat treatment. Therefore, the improvement in water repellency after heat treatment should not be simply attributed to a further increase in roughness. Instead, the laser-induced rough structure provides the necessary geometrical basis for air entrapment, while the heat-treatment-induced surface chemical changes, which will be discussed in the following section, further promote the transition toward a superhydrophobic state. The surface roughness parameters of the samples under different treatment conditions are summarized in Table 2.

Table 2. Surface roughness parameters of 3003 aluminum alloy surfaces under different treatment conditions.

Sample	Sa/μm	Sq/μm	Sz/μm	n
Untreated Al	0.31 ± 0.05	0.39 ± 0.05	2.59 ± 0.77	3
Heat-treated Al	0.27 ± 0.03	0.35 ± 0.02	2.56 ± 0.51	3
Laser-treated Al	0.42 ± 0.02	0.59 ± 0.003	5.49 ± 0.82	3
Laser + heat-treated Al	0.36 ± 0.04	0.51 ± 0.06	4.70 ± 0.41	3

Overall, the SEM observations and roughness measurements demonstrate that laser processing plays the dominant role in constructing the rough hierarchical surface morphology. The irregular micro-/nano-scale structures and increased peak–valley height favor the formation of trapped air pockets beneath water droplets, allowing the droplet to partially contact the solid surface. As a result, the apparent solid–liquid contact fraction is reduced, which facilitates the formation of a Cassie–Baxter wetting state. Recent studies have also emphasized that the wettability of laser-textured aluminum surfaces is governed by the combined effects of surface morphology, roughness, and surface chemistry rather than roughness alone [32].

3.7. Surface Chemical Composition and Functional Group Evolution

Because the laser-induced hierarchical structures were largely preserved after heat treatment, the improvement in surface wettability cannot be explained solely by changes in surface morphology [33]. Therefore, EDS and FTIR analyses were performed to investigate the evolution of the surface chemical composition and functional groups.

Table 3 summarizes the semi-quantitative elemental compositions of the laser-textured AA3003 surfaces before and after heat treatment. Before heat treatment, the surface consisted mainly of Al (82.62 wt.%), together with O (8.63 wt.%), C (7.61 wt.%), and Mn (1.13 wt.%). After heat treatment at 150 °C for 3 h, the carbon content increased markedly to 12.3 wt.%, whereas the oxygen content decreased from 8.63 to 7.6 wt.%. Meanwhile, the Al and Mn contents decreased slightly to 79.2 and 0.9 wt.%, respectively. Aluminum

and manganese originate primarily from the AA3003 substrate, whereas oxygen is associated with the naturally formed and laser-induced oxide layer. The detected carbon is mainly attributed to carbon-containing species adsorbed from the surrounding atmosphere [20].

Table 3. Semi-quantitative elemental compositions of laser-textured AA3003 surfaces before and after heat treatment.

Wt.%	C	O	Al	Mn	Total
Laser-textured Al	7.61	8.63	82.62	1.13	100.00
Laser + heat-treated Al	12.3	7.6	79.2	0.9	100.00

The increase in surface carbon, accompanied by a slight decrease in oxygen, indicates that heat treatment promotes the enrichment of carbon-containing species on the laser-textured surface. Similar changes in surface composition have been reported during the hydrophobic transition of laser-processed aluminum alloys [34]. Since EDS cannot distinguish the chemical bonding states of the detected elements, FTIR analysis was further carried out to identify the corresponding surface functional groups.

Figure 11a shows the vertically offset FTIR spectra of the as-received AA3003 sample (AR), heat-treated sample (HT), laser-textured sample without subsequent heat treatment (LT), laser-textured sample aged in ambient air for 7 days (LT-7d), and laser-textured and heat-treated sample (LT-HT). The AR and HT samples exhibit relatively weak spectral features, indicating that heat treatment alone causes no substantial change in the functional-group composition of the original AA3003 surface. In contrast, the laser-textured samples exhibit more distinct absorption features associated with the oxide/oxyhydroxide layer and adsorbed environmental species.

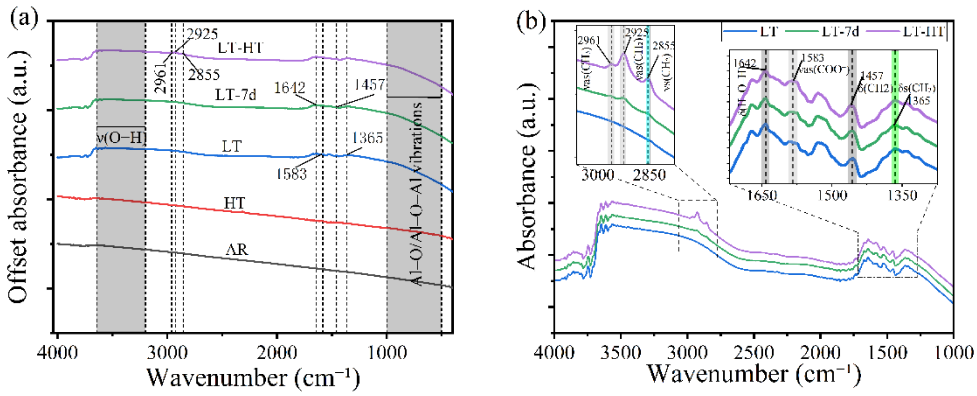


Figure 11. FTIR spectra of AA3003 surfaces subjected to different treatments. (**a**) Vertically offset FTIR spectra of the as-received sample (AR), heat-treated sample (HT), laser-textured sample without subsequent heat treatment (LT), laser-textured sample aged in ambient air for 7 days (LT-7d), and laser-textured and heat-treated sample (LT-HT). The spectra are vertically shifted for clarity. The vertical dotted lines in panel (**a**) indicate the positions of the characteristic absorption bands discussed in the text, while the dotted boxes and connecting lines in panel (**b**) indicate the spectral regions enlarged in the insets. (**b**) Comparison of the FTIR spectra of the LT, LT-7d, and LT-HT samples, with enlarged views of the C–H stretching region and the 1700–1300 cm^{-1} region.

The broad band in the 3200–3600 cm^{-1} region is assigned to O–H stretching vibrations arising from surface Al–OH groups, aluminum oxyhydroxides, and adsorbed water [35]. The broad absorption below approximately 1000 cm^{-1} is mainly attributed to Al–O and Al–O–Al lattice vibrations in aluminum oxides and oxyhydroxides [36]. These bands confirm that laser processing produces an oxidized and hydroxylated surface. However, the sharp

fluctuations at the high-wavenumber side of the O–H region may also contain contributions from residual atmospheric water vapor and should therefore be interpreted cautiously.

The enlarged C–H stretching region in Figure 11b shows characteristic bands at approximately 2961, 2925, and 2855 cm^{-1}, which are assigned to the asymmetric stretching vibration of CH_3 groups, the asymmetric stretching vibration of CH_2 groups, and the symmetric stretching vibration of CH_2 groups, respectively [37,38]. These bands provide direct evidence for the presence of aliphatic hydrocarbon species on the laser-textured surfaces. Compared with the freshly laser-textured sample, the C–H bands become more evident after 7 days of ambient aging and after heat treatment, indicating that both processes facilitate the adsorption, rearrangement, or stabilization of low-surface-energy carbonaceous species. This observation is consistent with the EDS result showing an increase in surface carbon after heat treatment.

In the 1700–1300 cm^{-1} region, the band near 1642 cm^{-1} is mainly assigned to the H–O–H bending vibration of adsorbed water [36]. The feature at approximately 1583 cm^{-1} is tentatively attributed to the asymmetric stretching vibration of surface carboxylate species, although contributions from other oxygen-containing carbonaceous species cannot be excluded. The band near 1457 cm^{-1} is associated primarily with CH_2 scissoring vibrations and may overlap with the symmetric stretching vibration of COO^- or vibrations of surface carbonate species. The band at approximately 1365 cm^{-1} is mainly assigned to the symmetric deformation vibration of CH_3 groups, with a possible contribution from carbonate-containing species. These results indicate the coexistence of polar oxygen-containing groups and non-polar hydrocarbon groups on the laser-textured surface.

The combined EDS and FTIR results indicate that laser processing initially generates an oxidized surface rich in Al–O and Al–OH species. During ambient aging or heat treatment, hydrocarbon-containing species are gradually enriched on the laser-textured surface, as evidenced by the increased carbon content and the enhanced CH_2 and CH_3 absorption bands. The enrichment of these non-polar species reduces the surface free energy and consequently decreases the affinity of the surface for water [20,31,39].

Consequently, the superhydrophobicity of the laser-textured and heat-treated AA3003 surface arises from the combined effects of the laser-generated hierarchical structures and the heat-induced evolution of surface chemistry. The rough surface provides the structural basis for minimizing liquid-solid contact, while the enrichment of hydrocarbon species lowers the surface free energy. Together, these effects promote the formation of a Cassie–Baxter-type wetting state [31,39], resulting in a water contact angle of 154.3 ± 0.8°.

3.8. Self-Cleaning Performance and Wettability Retention

The self-cleaning behavior and short-term wettability retention of the fluorine-free laser-textured AA3003 surface were evaluated through an SiO_2 powder-removal test, repeated gravity-driven water-impact testing, and tape-peeling testing. These experiments were intended to provide a preliminary assessment under the specified laboratory conditions rather than a comprehensive evaluation of long-term abrasion resistance or service durability.

3.8.1. Powder-Based Self-Cleaning Performance

To evaluate the powder-removal performance of the fluorine-free superhydrophobic AA3003 surface, SiO_2 powder with an average particle size of approximately 1 μm was used as a model contaminant. Before testing, the powder was dried to minimize the effects of adsorbed moisture and particle agglomeration. The designated regions of the untreated and superhydrophobic samples were uniformly covered with SiO_2 powder. The samples

were then fixed at an inclination angle of approximately 10°, and deionized water was dispensed using a 20 μL microsyringe.

Each water droplet had a volume of approximately 10–15 μL. The droplets were applied sequentially to the upper part of the contaminated region, allowing them to move downward under gravity. Under the present experimental conditions, near-complete removal of the SiO_2 powder from the superhydrophobic surface was generally achieved after approximately eight droplets, corresponding to a total applied water volume of approximately 80–120 μL.

The progressive cleaning behavior is shown in Figure 12. For the superhydrophobic surface, the water droplets retained a relatively compact shape and moved across the inclined sample while collecting and transporting SiO_2 particles. A visibly cleaned pathway gradually developed as the number of applied droplets increased, and only a small amount of powder remained after the eighth droplet. In contrast, water applied to the untreated AA3003 surface spread more extensively and remained pinned within the contaminated region. The interaction between the spreading water and SiO_2 powder produced wet particle agglomerates, and a considerable amount of contaminant remained even after the same number of droplets had been applied.

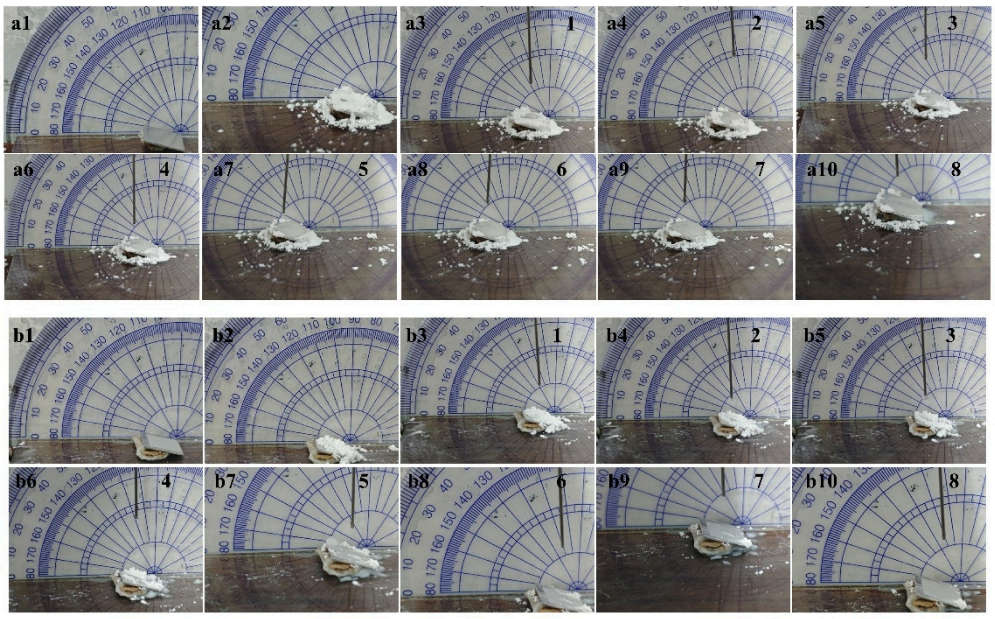


Figure 12. Comparison of powder self-cleaning behavior on untreated (**a1**–**a10**) and superhydrophobic (**b1**–**b10**) AA3003 surfaces. Panels (**a1**,**b1**) show the initially clean surfaces; panels (**a2**,**b2**) show the surfaces after being covered with SiO_2 powder; and panels (**a3**–**a10**,**b3**–**b10**) show the surfaces after the successive application of 1–8 deionized-water droplets, respectively. Each droplet had a volume of approximately 10–15 μL. The numbers 1–8 indicate the cumulative number of droplets applied.

To quantitatively compare the final powder-removal performance, the residual SiO_2-covered areas were analyzed using ImageJ. Because the initially contaminated areas differed between the two samples, the measured residual areas were normalized to their respective initial contaminated areas. The SiO_2 removal efficiency, η, was calculated as follows:

$$\eta = \left(1 - \frac{A_r}{A_0}\right) \times 100\%$$

where A_0 is the initially contaminated area and A_r is the residual SiO_2-covered area after water-assisted cleaning. The initial analyzed areas were 64 mm^2 for the superhydrophobic region and 100 mm^2 for the untreated AA3003 surface.

As shown in Figure 13(a1,a2), most of the SiO_2 powder was removed from the superhydrophobic region after water-droplet cleaning, with only several isolated residues remaining near the edges of the processed area. The measured residual SiO_2 area was 0.769 mm^2, corresponding to a residual coverage of 1.20% and a removal efficiency of 98.80%.

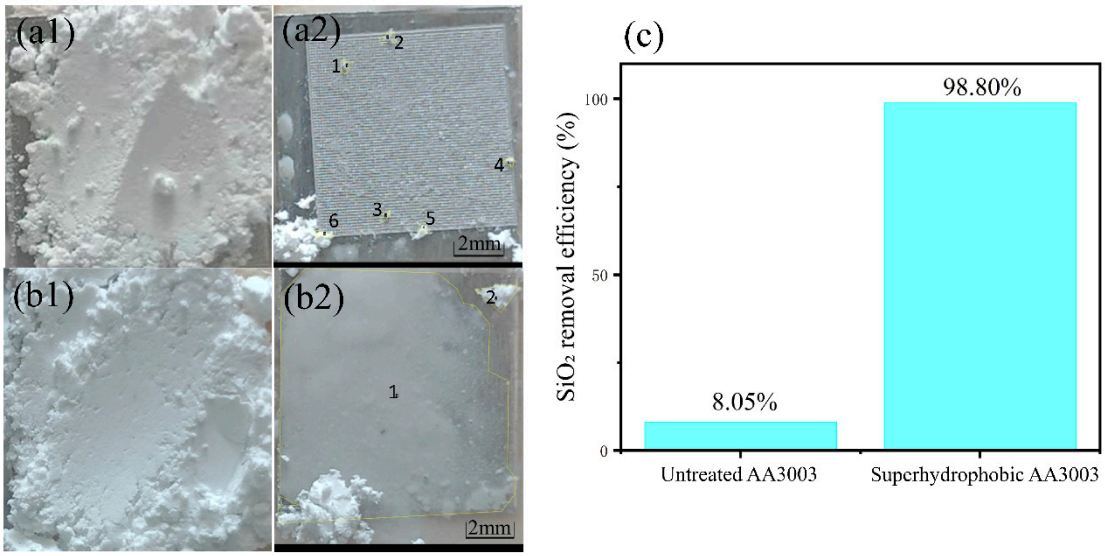


Figure 13. Powder-based self-cleaning performance of untreated and superhydrophobic AA3003 surfaces: (**a1**,**a2**) superhydrophobic surface before and after water-droplet cleaning, respectively; (**b1**,**b2**) untreated AA3003 surface before and after cleaning, respectively; and (**c**) comparison of the normalized SiO_2 removal efficiencies. The yellow outlines and numerical labels in (**a2**,**b2**) indicate the residual SiO_2 regions identified using ImageJ.

The improved self-cleaning behavior of the superhydrophobic surface is associated with its reduced affinity for water and multiscale surface topography. The relatively low effective solid–liquid contact fraction limits droplet spreading and pinning, allowing the moving droplets to collect and transport loosely attached SiO_2 particles. Conversely, the stronger water adhesion on untreated AA3003 promotes droplet spreading, particle wetting, and agglomeration, thereby restricting contaminant removal.

These results demonstrate that the laser-textured and heat-treated AA3003 surface provides effective removal of micrometer-sized SiO_2 powder during an inclined water-droplet test. Nevertheless, the reported removal efficiencies and required droplet number are specific to the present model contaminant, inclination angle, droplet volume, and water-application procedure and should not be directly generalized to other contaminant or operating conditions.

3.8.2. Repeated Water-Impact Resistance

To evaluate the resistance of the fluorine-free superhydrophobic AA3003 surface to repeated water impact, approximately 400 mL of deionized water was released from a height of 30 ± 2 cm during each impact cycle. The water contact angle (WCA) was measured after predetermined numbers of impact cycles. Three replicate tests were conducted under identical conditions, and the results are reported as the mean $\pm$ standard deviation.

The theoretical water velocity immediately before impact was estimated using the free-fall equation:

$$v = \sqrt{2gh}$$

where v is the water velocity immediately before impact, g is the gravitational acceleration, and h is the release height. Assuming negligible initial velocity and air resistance, the

theoretical water velocity corresponding to a release height of 30 ± 2 cm was estimated to be 2.43 ± 0.08 m s^{-1}.

As shown in Figure 14c, the initial WCA of the superhydrophobic surface was 154.7 ± 0.6°. After 2, 6, 10, 14, 18, and 22 impact cycles, the WCA values were 154.4 ± 0.8°,153.1 ± 0.4°, 152.4 ± 0.6°, 151.5 ± 0.5°, 150.9 ± 0.9°, and 150.1 ± 0.3°, respectively. Thus, the mean WCA remained above 150° for up to 22 impact cycles, indicating that the surface retained its superhydrophobic wettability under the present test conditions.

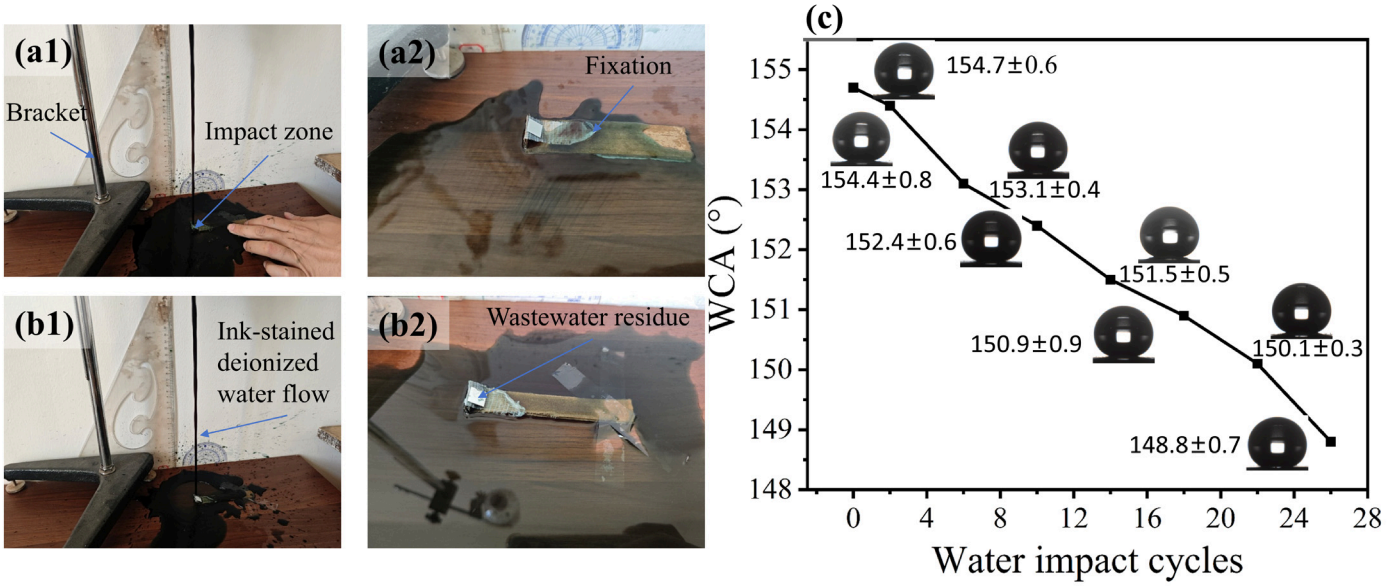


Figure 14. Water jet impact resistance of the fabricated surface: (**a1**,**a2**) liquid behavior on the untreated 3003 aluminum alloy surface; (**b1**,**b2**) liquid behavior on the superhydrophobic 3003 aluminum alloy surface; (**c**) variation in WCA with increasing water impact cycles.

After 26 impact cycles, the mean WCA decreased to 148.8 ± 0.7°. Although this value was slightly below the commonly used static WCA criterion of 150° for superhydrophobicity, it remained well above 90°, indicating that the surface still exhibited good hydrophobicity after 26 impact cycles [40]. Compared with the initial value, the mean WCA decreased by 5.9°, corresponding to a relative reduction of approximately 3.8%. This gradual decline indicates that repeated water impact caused a measurable but limited deterioration in surface wettability.

To further visualize the liquid repellency, dyed deionized water was used for comparative observations, as shown in Figure 14(a1,a2,b1,b2). On the untreated surface, the liquid spread over the surface and left obvious residues after impact, indicating strong liquid adhesion and poor water repellency. In contrast, on the superhydrophobic surface, the dyed water rapidly rolled or bounced away, and no obvious large-area residue was observed, demonstrating excellent water repellency and antifouling behavior.

The water jet impact resistance can be attributed to the synergistic effect of the hierarchical micro-/nano-structures and heat-treatment-induced surface chemical modification. The multi-scale rough structures facilitate air entrapment at the solid–liquid interface, reducing the effective contact area and preventing the formation of a stable water film during impact. Meanwhile, the modified surface chemistry helps reduce liquid adhesion, allowing impacting water to detach more easily from the surface. Therefore, the fabricated superhydrophobic surface maintains relatively high WCA and stable water repellency under repeated dynamic water impacts, indicating its potential for applications involving fluid exposure.

3.8.3. Tape Peeling Resistance

To evaluate the retention of water repellency under repeated adhesive-peeling conditions, a tape-peeling test was performed on the fabricated fluorine-free superhydrophobic AA3003 surface. Adhesive tape with a width of 1.5 cm was attached to the sample surface. A glass plate (10 cm × 10 cm) loaded with approximately 2 L of water was placed on the tape for 2 min to provide a relatively uniform normal pressure and ensure reproducible contact between the adhesive layer and the sample surface. The tape was subsequently removed at an approximately constant peeling rate.

Static water contact angles (WCAs) were measured after predetermined numbers of peeling cycles. The reported values are presented as the mean ± standard deviation of three measurements.

As shown in Figure 15b, the initial WCA of the superhydrophobic surface was 154.7 ± 0.7°. After one peeling cycle, the WCA remained at 154.4 ± 0.5°, indicating that a single adhesion–peeling operation produced only a minor change in surface wettability. As the number of peeling cycles increased to 5, 10, and 15, the WCA gradually decreased to 152.7 ± 0.6°, 151.3 ± 0.8°, and 150.5 ± 0.6°, respectively. Therefore, the mean WCA remained above the commonly adopted superhydrophobic threshold of 150° after 15 peeling cycles.

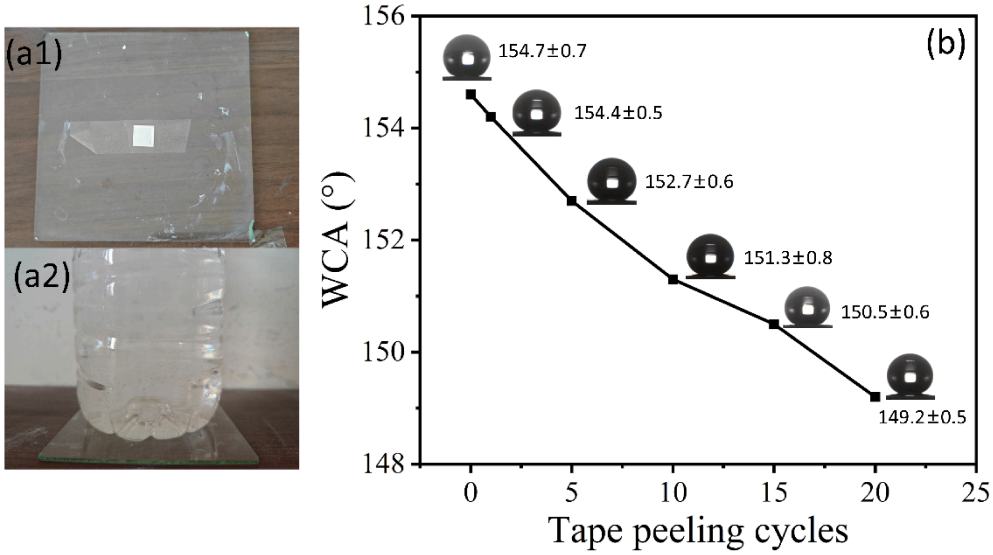


Figure 15. Tape peeling resistance of the superhydrophobic 3003 aluminum alloy surface: (**a1**) adhesive tape attached to the sample surface; (**a2**) loading process during tape attachment; (**b**) variation in WCA with increasing tape-peeling cycles.

After 20 peeling cycles, the WCA decreased to 149.2 ± 0.5°. Although this value was slightly below the static-WCA criterion generally used to define superhydrophobicity, the surface still exhibited pronounced hydrophobic behavior. Relative to the initial value, the total decrease in mean WCA was approximately 5.5°, corresponding to a reduction of about 3.6%.

The gradual decrease in WCA may be associated with partial damage to mechanically fragile protrusions, removal of weakly attached redeposited particles or carbon-containing surface species, and possible transfer of adhesive residues onto the textured surface. These effects may increase the effective solid–liquid contact fraction and reduce the ability of the textured surface to retain air beneath a water droplet.

Nevertheless, the relatively limited decrease in WCA indicates that the principal laser-generated multiscale topography remained largely preserved throughout the tape-peeling

procedure. Consequently, the fabricated surface retained a high degree of water repellency under repeated adhesive-peeling conditions.

It should be noted that tape-peeling performance is influenced by the adhesive type, peeling angle, peeling rate, applied pressure, and environmental conditions. Therefore, the present experiment should be regarded as a comparative laboratory-scale evaluation rather than a standardized measurement of long-term abrasion resistance or mechanical durability.

4. Conclusions

In this study, a fluorine-free fabrication route combining nanosecond laser texturing and subsequent heat treatment was employed to prepare highly water-repellent surfaces on AA3003 aluminum alloy. The effects of scanning speed, laser power, pulse frequency, and scanning interval on surface wettability were systematically investigated.

The results showed that the optimal processing conditions were a scanning speed of 2700 mm/s, laser power of 6 W, pulse frequency of 35 kHz, and scanning interval of 20 μm. Under these conditions, the laser-textured and heat-treated surface exhibited a maximum static water contact angle of 154.3 ± 0.8°.

Surface characterization revealed that nanosecond laser processing generated hierarchical micro-/nano-scale structures composed of grooves, pits, resolidified particles, and protrusions, resulting in increased surface roughness. Subsequent heat treatment preserved the laser-induced rough morphology while promoting surface chemical evolution, as evidenced by the increase in surface carbon content and the enhanced C–H-related absorption bands observed in FTIR spectra. The combined effects of hierarchical roughness and heat-treatment-associated surface chemical changes contributed to the development of the highly water-repellent state.

The fabricated surface exhibited effective powder-removal behavior during inclined water-droplet tests, achieving a SiO_2 removal efficiency of 98.8% under the specified experimental conditions. In addition, the surface retained relatively high water repellency during repeated water-impact and tape-peeling tests. The static water contact angle remained above 150° after 22 water-impact cycles and after 15 tape-peeling cycles. Even after 26 water-impact cycles and 20 tape-peeling cycles, the contact angles remained at 148.8 ± 0.7° and 149.2 ± 0.5°, respectively.

Overall, the present results demonstrate that the combination of nanosecond laser texturing and heat treatment provides an effective fluorine-free strategy for fabricating highly water-repellent AA3003 aluminum alloy surfaces. The prepared surfaces showed promising self-cleaning behavior and short-term wettability retention under the investigated laboratory conditions, indicating potential for antifouling and surface-protection applications. Further studies involving abrasion resistance, corrosion performance, ultraviolet aging, and long-term outdoor exposure are required to evaluate practical service durability.

Author Contributions: Conceptualization, Z.L. and J.Z.; methodology, J.Z. and H.L.; validation, J.Z. and H.L.; formal analysis, H.L.; investigation, J.Z. and H.L.; data curation, H.L.; writing—original draft preparation, H.L. and J.Z.; writing—review and editing, H.L. and Z.L.; visualization, H.L.; supervision, Z.L.; project administration, Z.L. All authors have read and agreed to the published version of the manuscript.

Funding: This research received no external funding. The APC was funded by J.Z.

Institutional Review Board Statement: Not applicable.

Informed Consent Statement: Not applicable.

Data Availability Statement: The data presented in this study are available on request from the corresponding author.

Acknowledgments: The authors would like to thank Harbin University of Commerce for experimental support. During the preparation of this manuscript, the authors used ChatGPT (GPT-5.5 and GPT-5.6) for English language polishing and formatting assistance. The authors have reviewed and edited the output and take full responsibility for the content of this publication.

Conflicts of Interest: The authors declare no conflicts of interest.

References

1. Tan, Y.B.; Wang, X.M.; Ma, M.; Zhang, J.X.; Liu, W.C.; Fu, R.D.; Xiang, S. A study on microstructure and mechanical properties of AA 3003 aluminum alloy joints by underwater friction stir welding. *Mater. Charact.* **2017**, *127*, 41–52. [CrossRef]
2. Gao, Z.; Qin, Z.; Lu, Q. Controlled atmosphere brazing of 3003 aluminum alloy using low-melting-point filler metal fabricated by melt-spinning technology. *Materials* **2022**, *15*, 6080. [CrossRef] [PubMed]
3. Lu, Q.; Zhao, Y.; Wang, Q.; Li, D. Investigation on the corrosion resistance of 3003 aluminum alloy in acidic salt spray under different processing states. *Metals* **2024**, *14*, 196. [CrossRef]
4. Karapanagiotis, I. Superhydrophobic and superoleophobic surfaces: Key points, challenges and applications. *Coatings* **2023**, *13*, 551. [CrossRef]
5. Feng, L.; Zhang, Y.; Xi, J.; Zhu, Y.; Wang, N.; Xia, F.; Jiang, L. Petal effect: A superhydrophobic state with high adhesive force. *Langmuir* **2008**, *24*, 4114–4119. [CrossRef] [PubMed]
6. Bhushan, B.; Nosonovsky, M. The rose petal effect and the modes of superhydrophobicity. *Philos. Trans. R. Soc. A* **2010**, *368*, 4713–4728. [CrossRef] [PubMed]
7. Parra-Vicente, S.; Ibáñez-Ibáñez, P.F.; Cabrerizo-Vílchez, M.; Sánchez-Almazo, I.; Rodríguez-Valverde, M.Á.; Montes Ruiz-Cabello, F.J. Understanding the petal effect: Wetting properties and surface structure of natural rose petals and rose petal-derived surfaces. *Colloids Surf. B Biointerfaces* **2024**, *236*, 113832. [CrossRef] [PubMed]
8. Khan, M.Z.; Militky, J.; Petru, M.; Tomková, B.; Ali, A.; Tören, E.; Perveen, S. Recent advances in superhydrophobic surfaces for practical applications: A review. *Eur. Polym. J.* **2022**, *178*, 111481. [CrossRef]
9. Zhang, Y.; Zhang, Z.; Yang, J.; Yue, Y.; Zhang, H. A review of recent advances in superhydrophobic surfaces and their applications in drag reduction and heat transfer. *Nanomaterials* **2022**, *12*, 44. [CrossRef] [PubMed]
10. Liravi, M.; Pakzad, H.; Moosavi, A.; Nouri-Borujerdi, A. A comprehensive review on recent advances in superhydrophobic surfaces and their applications for drag reduction. *Progress. Org. Coat.* **2020**, *140*, 105537. [CrossRef]
11. Kataria, S.; Sikarwar, B.S.; Kumar, R.; Muralidhar, K. Influence of wettability design on moist air condensation: Superhydrophobic, unidirectional wettability gradient and patterned surfaces. *Int. Commun. Heat Mass Transf.* **2026**, *175*, 111017. [CrossRef]
12. Zhang, W.; Wang, D.; Sun, Z.; Song, J.; Deng, X. Robust superhydrophobicity: Mechanisms and strategies. *Chem. Soc. Rev.* **2021**, *50*, 4031–4061. [CrossRef] [PubMed]
13. Quan, Y.; Chen, Z.; Lai, Y.; Huang, Z.; Li, H. Recent advances in fabricating durable superhydrophobic surfaces: A review in the aspects of structures and materials. *Mater. Chem. Front.* **2021**, *5*, 1655–1682. [CrossRef]
14. Zeng, Q.; Zhou, H.; Huang, J.; Guo, Z. Review on the recent development of durable superhydrophobic materials for practical applications. *Nanoscale* **2021**, *13*, 11734–11764. [CrossRef] [PubMed]
15. Xavier, J.R.; Vinodhini, S.P. Advanced nanocomposite coatings of aluminum alloys for enhanced corrosion, flame retardancy, and mechanical strength applied to aerospace manufacturing. *Colloids Surf. A Physicochem. Eng. Asp.* **2024**, *698*, 134543. [CrossRef]
16. Zeng, Q.; Min, X.; Luo, Z.; Dai, H. In-situ fabrication of superhydrophobic Zn–Al layered double hydroxide coating on aluminum alloys for corrosion protection. *Mater. Lett.* **2022**, *328*, 133077. [CrossRef]
17. Kwon, H.M.; Lee, S.J.; Kim, C.L. Durable superhydrophobic stainless steel via two-step chemical etching and fluoro-silane coating. *Mater. Chem. Phys.* **2025**, *339*, 130743. [CrossRef]
18. Wei, J.; Xin, B.; Liu, J.; Wang, P.; Lei, T.; Jing, N. A robust superhydrophobic Al_2O_3/PU coating via KH-550-assisted anchoring of SiO_2-PTFE. *Appl. Surf. Sci.* **2026**, *728*, 166012. [CrossRef]
19. Li, G.; Li, L.; Huang, B.; Luo, K.; Xie, Y.; Xu, T.; Wu, W. Wear-resistant superhydrophobic coating: Ice adhesion fabrication, performance evaluation, and mechanism. *Polymers* **2026**, *18*, 1077. [CrossRef] [PubMed]
20. Ngo, C.-V.; Liu, Y.; Li, W.; Yang, J.; Guo, C. Scalable wettability modification of aluminum surface through single-shot nanosecond laser processing. *Nanomaterials* **2023**, *13*, 1392. [CrossRef] [PubMed]
21. Volpe, A.; Covella, S.; Gaudiuso, C.; Ancona, A. Improving the laser texture strategy to get superhydrophobic aluminum alloy surfaces. *Coatings* **2021**, *11*, 369. [CrossRef]
22. Sun, Z.; Zhao, X.; Yuan, J.; Kong, G.; Lai, D.; Zheng, Y. Fabrication of hybrid micro-nano structure superhydrophobic surfaces by a simple nanosecond laser ablation and chemical modification process. *Mater. Chem. Phys.* **2025**, *334*, 130480. [CrossRef]
23. Yang, Q.; Xu, Z.; Yi, Z.; Sun, L.; Cheng, J.; Chen, L.; Lou, D.; Li, Q.; Liu, D. Fabrication of superhydrophobic surface on aluminum alloy via dual-role nanosecond laser ablation and induction. *J. Mater. Eng. Perform.* **2025**, *35*, 16714–16730. [CrossRef]

24. Wang, J.Q.; Xu, Y.H.; Gao, Y.L.; Yan, Y.D.; Geng, Y.Q. Environmentally friendly approaches and mechanisms for hydrophobic transition of metals via nanosecond laser processing. *Chin. J. Surf. Eng.* **2025**, *38*, 42–63. [CrossRef]
25. Ifwar, F.; Mandal, P.; Arora, H.S. Eco-friendly and facile fabrication of superhydrophobic aluminum alloys. *Proc. Inst. Mech. Eng. Part J J. Eng. Tribol.* **2022**, *236*, 259–265. [CrossRef]
26. Zschach, L.G.; Soldera, F.; Marzec, M.; Sokołowski, K.; Sallese, M.; Lasagni, A.F.; Baumann, R. Laser texturing of AA2024 alloy: A simplified approach to improve corrosion resistance and achieve superhydrophobicity. *Surf. Coat. Technol.* **2025**, *513*, 132487. [CrossRef]
27. Liu, D.; Liu, R.; Cao, L.; Bryanston-Cross, P.J.; Zhang, Z.; Wang, Z. Nanosecond laser interference ablation of fluorine-free aluminum alloy surfaces for dynamic adhesion and static wettability synergistically modulating water collection. *Colloids Surf. A Physicochem. Eng. Asp.* **2025**, *705*, 135696. [CrossRef]
28. Cholkar, A.; Chatterjee, S.; Jose, F.; O'Connor, R.; McCarthy, É.; Weston, N.; Kinahan, D.; Brabazon, D. Parametric investigation of ultrashort pulsed laser surface texturing on aluminium alloy 7075 for hydrophobicity enhancement. *Int. J. Adv. Manuf. Technol.* **2024**, *130*, 4169–4186. [CrossRef] [PubMed]
29. Farhan, H.; Ishak, M.; Rai, R.; Quazi, M.M.; Halil, A.B.M. Development of laser-textured hydrophobic surfaces on aluminum 6061 using a low-cost laser marker. *J. Mater. Eng. Perform.* **2026**, *35*, 16644–16657. [CrossRef]
30. Cheng, K.; Wang, J.; Xu, B.; Wang, G. Study on the fabrication of coating-free superhydrophobic aluminum alloy surfaces by femtosecond laser and its wettability control mechanism. *Nanomaterials* **2026**, *16*, 237. [CrossRef] [PubMed]
31. Qahtani, F.; Shrotriya, P. Tuning the Wettability of a High-Strength Aluminum Alloy Using a Picosecond Laser and Stearic Acid Coating. *Coatings* **2023**, *13*, 1939. [CrossRef]
32. Zschach, L.G.; Ränke, F.; Tabares, I.; Baumann, R.; Soldera, F.; Soldera, M.; Lasagni, A.F. Long-term corrosion performance of superhydrophobic vs. superhydrophilic laser-modified AA2024 surfaces under ambient storage. *npj Mater. Degrad.* **2025**, *9*, 127. [CrossRef]
33. Zhou, J.; Wu, J.; Tang, S.; Li, Y. Review of Laser Texturing Technology for Surface Protection and Functional Regulation of Aluminum Alloys: Wettability, Anti-Icing, Corrosion Resistance, and Wear Resistance. *Coatings* **2025**, *15*, 567. [CrossRef]
34. Zhao, M.; Guo, J.; Zhao, J.; Guo, Z.; Shrotriya, P.; Cui, Y.; Yang, Z. Heat Treatment Temperature Effect on Wettability of Laser-Machined Aluminum Surface. *J. Mater. Eng. Perform.* **2022**, *31*, 733–741. [CrossRef]
35. Ludwig, B.; Burke, T.T. Infrared Spectroscopy Studies of Aluminum Oxide and Metallic Aluminum Powders, Part I: Thermal Dehydration and Decomposition. *Powders* **2022**, *1*, 47–61. [CrossRef]
36. Gholizadeh, Z.; Aliannezhadi, M.; Ghominejad, M.; Shariatmadar Tehrani, F. High Specific Surface Area γ-Al_2O_3 Nanoparticles Synthesized by Facile and Low-Cost Co-Precipitation Method. *Sci. Rep.* **2023**, *13*, 6131. [CrossRef] [PubMed]
37. Ryu, C.; Kim, H.; Lee, H.; In, J.B. Laser-Induced Selective Wettability Transition of 6061 Aluminum Alloy Surfaces. *J. Mech. Sci. Technol.* **2024**, *38*, 2143–2150. [CrossRef]
38. Yuan, G.; Liu, Y.; Ngo, C.-V.; Guo, C. Rapid Fabrication of Anti-Corrosion and Self-Healing Superhydrophobic Aluminum Surfaces through Environmentally Friendly Femtosecond Laser Processing. *Opt. Express* **2020**, *28*, 35636–35650. [CrossRef] [PubMed]
39. Sarkiris, P.; Ellinas, K.; Gogolides, E. Durable Superhydrophobic Aluminum Surfaces against Immersion and Hot Steam Impact: A Comparative Evaluation of Different Hydrophobization Methods and Coatings. *Coatings* **2024**, *14*, 908. [CrossRef]
40. Law, K.Y. Definitions for Hydrophilicity, Hydrophobicity, and Superhydrophobicity: Getting the Basics Right. *J. Phys. Chem. Lett.* **2014**, *5*, 686–688. [CrossRef] [PubMed]

Disclaimer/Publisher's Note: The statements, opinions and data contained in all publications are solely those of the individual author(s) and contributor(s) and not of MDPI and/or the editor(s). MDPI and/or the editor(s) disclaim responsibility for any injury to people or property resulting from any ideas, methods, instructions or products referred to in the content.